

Angular Glint Error Simulation Using Attributed Scattering Center Models

KUN-YI GUO¹, (Member, IEEE), GUANG-LIANG XIAO, YUN ZHAI,
AND XIN-QING SHENG¹, (Senior Member, IEEE)

Center for Electromagnetic Simulation, Beijing Institute of Technology, Beijing 100081, China

Corresponding author: Kun-yi Guo (guokunyi@bit.edu.cn)

This work was supported by the National Natural Science Foundation of China under Grants 61471041 and 61771052.

ABSTRACT Angular glints are induced essentially by the superposition of scattering responses from multiple scattering centers and usually fluctuate quickly and widely with the aspect angles for complex targets change. This paper presents angular glint simulation of complex conducting targets using attributed scattering centers. The formulae for linear glint errors (LGEs) are derived based on the parametric models of attributed scattering centers and can be applied for real-time LGE simulation. Our analyses and numerical experiments show that the LGE simulation requires more precise scattering center modeling than the radar imaging simulation does. To ensure the accuracy of the LGE simulation, a forward approach that uses induced currents on conducting targets is used to precisely extract the scattering centers. The numerical results show that the LGE simulation based on the developed scattering center model has high accuracy. More importantly, the scattering center model developed for sparse aspect angles can be used to simulate LGEs for dense aspect angles, as required for complex targets, which leads to high efficiency in simulating LGEs.

INDEX TERMS Angular glint, linear glint error, scattering center model.

I. INTRODUCTION

Parametric models and extraction methods for scattering centers have received considerable consideration in the fields of radar techniques and electromagnetic computation. Parametric models of scattering centers can characterize the radar returns of extended targets by using concise analytical functions, which lead to high efficiency for radar signal simulation and the post-processing of simulated signals. Furthermore, the physically relevant parameters of the scattering centers have great advantages in radar image interpretation and automatic target recognition (ATR) [1]–[3].

To establish a scattering center model for a complex target, there are usually two steps: the first is to find the appropriate functions (i.e., mathematic models) to describe the scattering characteristics of the scattering centers, and the second is to extract the parameters of the scattering centers from radar images of the targets. The existing models for scattering centers include the damped exponential model [4], [5], the geometrical theory of diffraction (GTD)-based model [6], the attributed scattering center model [7] [8], the canonical scattering feature models for bistatic radar [9], the sliding scattering center model [10], [11], and the creeping wave scattering center model [12].

The extraction methods include inverse methods and forward methods. For inverse methods, the scattering centers are extracted from synthetic aperture radar (SAR) images [13]–[16], or from the scattering fields using the super resolution technique [17], [18] and the optimal estimating method [19]. The forward methods [20], [21] usually involve two steps. In the first, the geometric structure of the target is divided into appropriate partitions, and the scattered fields of each partition (the scattering contribution of the scattering center) are computed using high-frequency methods, such as physical optics (PO), GTD, equivalent electromagnetic currents (EEC), and incremental length diffraction coefficients (ILDC). In the second step, the parameters of the scattering center models are extracted by fitting the parametric models.

Scattering center models have been successfully applied in radar imaging and recognition. In this work, scattering centers are applied in angular glint error (AGE) simulations for radar angular measurements. AGE, which is induced essentially by the superposition of scattering fields from multiple scattering centers of the detected target [22], is one of the main errors in radar angular measurements. AGEs are generally investigated numerically through linear glint errors (LGE) along two orthogonal directions. Two commonly used methods for

LGE computation are the phase gradient method (PGM) and the Poynting vector method (PVM) [23], [24].

Based on these methods, formulae for LGEs that are easier to operate have been proposed [25]–[28]. Among them, the formulae for ideal scatterers are the most effective for LGE simulation. However, the simulation precision is very low. For real targets, scattering centers are far more complex than ideal scatterers and have complex attributes; e.g., their locations and scattering amplitudes depend closely on the aspect angles of line of sight (LOS). To address this issue, formulae are derived for complex targets according to the attributes of real scattering centers in this work.

LGE is extremely sensitive to changes in the locations and scattering amplitudes of the scattering centers. In contrast to the simulation of radar imaging, weak scattering centers can greatly affect LGEs. Therefore, LGE simulation requires more precise scattering center parameters than radar imaging simulation does. To achieve high-precision scattering center extraction, an approach that uses induced currents is proposed in this work. The parameters of individual scattering centers are extracted from their contributing partitions of currents rather than from the total fields of the target. Therefore, the errors induced by interference from other scattering centers are effectively avoided. Based on the extracted scattering centers and the derived LGE formulae, the influence that different types of scattering centers have on LGE is investigated in detail. This investigation has led to some meaningful conclusions, which are helpful in interpreting the fluctuant features of LGEs and understanding their negative correlations with radar cross sections (RCS).

To validate the presented LGE simulation approach, the scattering centers and LGEs of an unmanned aerial vehicle (UAV), are investigated as an example. The extracted models of scattering centers are validated by comparing the RCSs and time-frequency representations (TFR) of scattered waves that are simulated by the models with those computed by the full-wave numerical method called parallel multilevel fast multipole algorithm (PMLFMA) [29]. The LGEs calculated by the formulae are compared with those calculated by brute-force computation. The numerical results show that the proposed LGE simulation approach has high accuracy and efficiency.

The remainder of this paper is organized as follows: Section II presents the formulae of the LGEs, which are derived from the attributed scattering centers; Section III presents an analysis of the relationship between the attributed scattering centers and LGEs; Section IV presents the scattering center extraction approach for complex targets using induced currents; Section V presents the validations; and Section VI presents the conclusions drawn from this work.

II. FORMULAE OF LGEs DESCRIBED BY SCATTERING CENTER MODEL

The scattering centers can be classified into three types according to their various attributes: localized scattering centers (LSCs), distributed scattering centers (DSCs) and sliding

scattering centers (SSCs) [30]. Their scattering amplitudes and locations are dependent, in quite different ways, on the aspect angles and frequencies of the incident radar waves. The detailed properties of these three types of scattering centers are presented in appendix A.

The geometries of the radar and target are shown in Fig. 1. A body-fixed Cartesian coordinate system, with unit vectors $(\hat{x}, \hat{y}, \hat{z})$, is used here to describe the locations of the scattering centers and radar, and a spherical coordinate system, with unit vectors $(\hat{r}, \hat{\theta}, \hat{\phi})$, is used to describe the directions of the electric and magnetic fields. The position vector of the i th scattering center and radar vector are denoted by \mathbf{r}_i and \mathbf{r}_{los} , respectively. For SSC, \mathbf{r}_i changes with the aspect angle of the LOS.

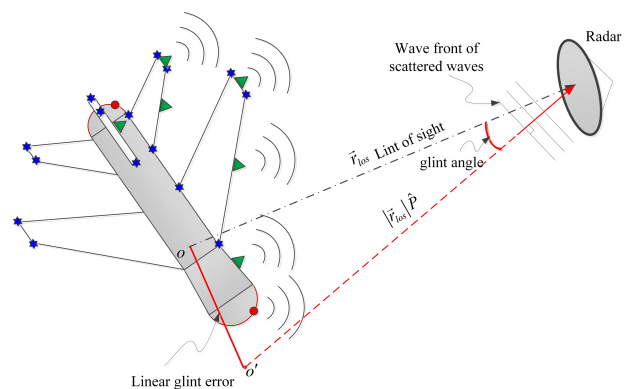


FIGURE 1. Geometry of the target and radar.

The scattering center model for a monostatic radar system configuration can be expressed by Eq. (1). Linear polarizations of the transmitter and the receiver are only considered here. The scattering center models generally do not consider the cross-polarization components of scattering centers, therefore the expression of the scattering fields of scattering centers under VV polarization is used in the following derivation.

$$E(f, \Psi) = \sum_i^n A_i(\Psi) e^{j\varphi_i} \left(\frac{jf}{f_c}\right)^{\alpha_i} \exp(-j2kR_i(\Psi)) (\hat{\theta}_i \cdot \hat{\theta}_{los}) \quad (1)$$

where $\Psi = (\theta_{los}, \phi_{los})$ denotes the aspect angle of $\hat{\mathbf{r}}_{los}$; $A_i(\Psi)$ and φ_i are the scattering amplitude and initial phase of the i th scattering center, and they have different expressions for LSC, DSC and SSC; $R_i(\Psi)$ is the distance between the scattering center and the radar, which can be described as $R_i(\Psi) = |\mathbf{r}_{los}(\Psi) - \mathbf{r}_i(\Psi)|$; $\hat{\theta}_i$ denotes the direction of the electric field of the scattered wave; and α is the frequency dependent factor and varies according to the scattering mechanism such that $\alpha = 1$ for the scattering center induced by the specular reflection from a planar surface, $\alpha = 0.5$ for the scattering center induced by the reflection from a single-curved surface, $\alpha = 0$ for the scattering center induced by the reflection from a doubly curved surface, or a straight

edge, and $\alpha = -1$ for the scattering center induced by the diffraction from end points.

The above values of α are derived from the solutions of canonical targets under high-frequency conditions. In our case, scattering contributions under lower frequencies are also considered. Considering that the scattering waves under single frequency is only involved in this work, we set α as an unknown parameter for the lower frequency cases through the optimal matching into the real scattered fields. The values for the high-frequency case are set as the initial values in the matching process.

From the geometry of the radar and the scattering centers, it is easy to show that $\hat{\theta}_i \cdot \hat{\theta}_{los} = \frac{\mathbf{r}_{los} \cdot (\mathbf{r}_{los} - \mathbf{r}_i)}{|\mathbf{r}_{los} \cdot (\mathbf{r}_{los} - \mathbf{r}_i)|}$. For far-field conditions, $r_i \ll r_{los}$, so $\hat{\theta}_i \cdot \hat{\theta}_{los} \approx 1$; i.e., $\hat{\theta}_i$ is much closer to $\hat{\theta}_{los}$. Therefore, the part $\hat{\theta}_i \cdot \hat{\theta}_{los}$ in the amplitude is ignored when modeling the scattering centers under far field conditions. However, the directions of the electric and magnetic fields, $\hat{\theta}_i$ and $\hat{\phi}_i$, should be considered in the analysis of LGEs.

Assuming that the waves scattered from scattering centers can be described by spherical waves, the electromagnetic fields can be expressed as in Eqs. (2) and (3), where Ψ in $A_i(\Psi)$, $R_i(\Psi)$ is omitted only for convenience of expression.

$$\mathbf{E}(f, \Psi) = \sum_i^n \frac{A_i}{R_i} \left(\frac{f}{f_c}\right)^{\alpha_i} e^{j(\frac{\pi}{2}\alpha_i + \varphi_i)} \exp(-j2kR_i) \hat{\theta}_i \quad (2)$$

$$\mathbf{H}(f, \Psi) = \sum_i^n \frac{A_i}{\eta_0 R_i} \left(\frac{f}{f_c}\right)^{\alpha_i} e^{j(\frac{\pi}{2}\alpha_i + \varphi_i)} \exp(-j2kR_i) \hat{\phi}_i \quad (3)$$

where η_0 is the wave impedance of free space. $\hat{\theta}_i$ and $\hat{\phi}_i$ are given in Eq. (4).

$$\begin{aligned} \hat{\theta}_i &= \cos \theta_i \cos \phi_i \hat{\mathbf{x}} + \cos \theta_i \sin \phi_i \hat{\mathbf{y}} - \sin \theta_i \hat{\mathbf{z}} \\ \hat{\phi}_i &= -\sin \phi_i \hat{\mathbf{x}} + \cos \phi_i \hat{\mathbf{y}}. \end{aligned} \quad (4)$$

Then, according to PVM, the LGEs can be derived by Eqs. (5) and (6)). The derivations are given in appendix B.

$$e_\theta = r_{los} \tan(\Theta - \theta_{los}) \quad (5)$$

$$e_\phi = r_{los} \frac{\sin \Theta \tan(\Phi - \phi_{los})}{\cos(\Theta - \theta_{los})} \quad (6)$$

where Θ , Φ are given by Eq. (32) in appendix B.

From Eqs. (5) and (6), it can be concluded that e_θ is inherently determined by Θ , and e_ϕ by both Θ and Φ . The relationship between e_θ and e_ϕ can be derived as shown below:

$$e_\phi = (e_\theta + r_{los} \tan \theta_{los}) \cos \theta \tan(\Phi - \phi_{los}). \quad (7)$$

Eq. (7) shows that e_ϕ includes two parts. If $e_\theta \ll r_{los} \tan \theta_{los}$, then e_ϕ is mainly determined by Φ , as expressed below.

$$e_\phi \approx r_{los} \sin \theta_{los} \tan(\Phi - \phi_{los}) \quad (8)$$

From Eqs. (5) and (8), it can be inferred that the glint angles on the θ and ϕ planes are $\Delta\theta = \Theta - \theta_{los}$ and

$\Delta\phi = \Phi - \phi_{los}$, respectively. After the derivation presented in appendix B, we get

$$e_\theta = r_{los} \frac{\sum_i^n \sum_j^n g_{ij} \sin(\theta_i - \theta_{los})}{\sum_i^n \sum_j^n g_{ij} \cos(\theta_i - \theta_{los})} \quad (9)$$

$$\begin{aligned} e_\phi &= \frac{r_{los} \sum_i^n \sum_j^n g_{ij} \sin \theta_i}{\sum_i^n \sum_j^n g_{ij} \cos(\theta_i - \theta_{los})} \\ &\times \frac{\sum_i^n \sum_j^n g_{ij} \sin \theta_i \sin(\phi_i - \phi_{los})}{\sum_i^n \sum_j^n g_{ij} \sin \theta_i \cos(\phi_i - \phi_{los})} \end{aligned} \quad (10)$$

For far field conditions, the following amplitude parts can be approximated to give the following expressions:

$$\begin{aligned} \frac{1}{R_i R_j} &\approx \frac{1}{r_{los}^2} \\ \cos(\phi_j - \phi_{los}) &\approx 1 \\ \cos(\phi_i - \phi_j) &\approx 1 \\ \sin(\theta_i - \theta_{los}) &\approx r_i \sin(\theta'_i - \theta_{los}) \frac{1}{r_{los}} \\ \sin(\phi_i - \phi_{los}) &\approx r_i \sin \theta'_i \sin(\phi'_i - \phi_{los}) \frac{1}{r_{los}} \end{aligned} \quad (11)$$

where θ'_i , ϕ'_i are the Euler angles of vector \mathbf{r}_i . Then, Eqs. (9) and (10) can be simplified as shown below:

$$e_\theta \approx \frac{\sum_i^n \sum_j^n \bar{g}_{ij} r_i(\Psi) \sin(\theta'_i - \theta_{los})}{\sum_i^n \sum_j^n \bar{g}_{ij}} \quad (12)$$

$$e_\phi \approx \frac{\sum_i^n \sum_j^n \bar{g}_{ij} r_i(\Psi) \sin \theta'_i \sin(\phi'_i - \phi_{los})}{\sum_i^n \sum_j^n \bar{g}_{ij}} \quad (13)$$

where

$$\begin{aligned} \bar{g}_{ij} &= A_i(\Psi) A_j(\Psi) \left(\frac{f}{f_c}\right)^{(\alpha_i + \alpha_j)} \\ &\cdot \cos[2k(R_j(\Psi) - R_i(\Psi)) + \frac{\pi}{2}(\alpha_i - \alpha_j) + \varphi_i - \varphi_j] \end{aligned} \quad (14)$$

Although Eqs. (12) and (13) have similar computational complexity as Eqs. (9) and (10) do, they show clearer physical characteristics of LGEs under far field conditions; i.e., the LGEs are invariant with r_{los} (the distance between the radar and the target) in far field conditions. By contrast, LGEs depend closely on \hat{r}_{los} (the direction of the LOS). If the direction of the LOS is invariant, the changes in distance have little effect on the linear errors. Conversely, LGEs are sensitive to changes in the direction of the LOS, even if the distance is invariant. These results agree well with the existing conclusions drawn from LGEs computed by brute-force computation [23].

III. ANALYSIS OF THE RELATIONSHIP BETWEEN ATTRIBUTED SCATTERING CENTERS AND LGEs

First, the variations in LGEs with changes in the locations and amplitudes of scattering centers are investigated using Eqs. (12) and (13). For numerical testing, two scatterers, located on the z axis symmetrically around the origin of the

coordinates system, are considered. The distance between the scatterers is d , and the ratio of their scattering amplitude is δ . The variations of LGE with changes in d are shown in Fig. 2, where $\delta = 2$, and those with changes in δ are shown in Fig. 3, where $d = 2\lambda$.

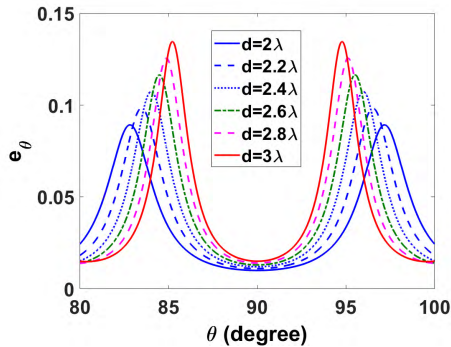


FIGURE 2. Change in LGEs with d .

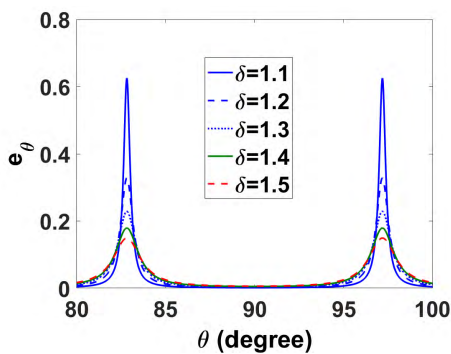


FIGURE 3. Change in LGEs with δ .

From these results, it can be seen that the smaller the scattering amplitude difference is and the greater the distance between multiple scattering centers is, the larger the LGEs are. The fluctuations in LGEs with the direction of LOS are extremely sensitive to the attributes of the scattering centers, such as their location and amplitude. Even a subtle change in distance, e.g., within one wavelength, can cause a significant change in LGE (see Fig. 3). Furthermore, the smaller the amplitude difference between two scattering centers is, the more sensitive the LGE is to changes caused by variations in the scattering amplitude. Therefore, high precision in scattering center modeling is essential for LGE simulation.

Second, the influence of the scattering center type for a real target is investigated here using a cone with curved generatrix, as shown in Fig. 4. Depending on the geometry of the target and previous knowledge of three types of scattering centers, it can easily be shown that the target has 5 scattering centers: 1 SSC, 3 LSCs (LSC1, LSC2, LSC3) and 1 DSC (see Fig. 4). The SSC is induced by reflection from the curved surface, the DSC by specular reflection from the bottom disk, the LSC1 by reflection from the top of the cone and the

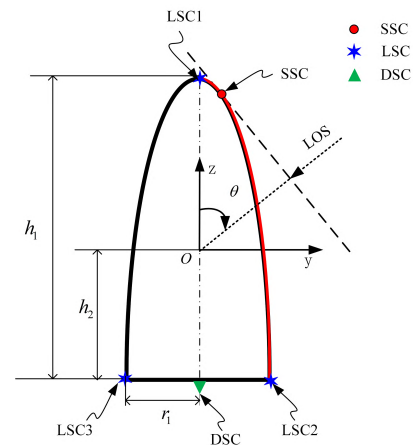


FIGURE 4. Geometry and scattering centers of the cone with curved generatrix.

LSC2 and LSC3 by waves diffracted from the curved edge in light and shadow regions, respectively.

The following are the geometric parameters of this target: $h_1 = 1.6 \text{ m}$, $r_1 = 0.4 \text{ m}$, and $h_2 = 0.6 \text{ m}$. The frequency of the scattered wave is 2 GHz , and the range of the observation angle is $\theta = 0 \sim 180^\circ$, $\phi = 90^\circ$. The target is assumed to rotate around the \hat{x} axis with an angular velocity of 2 rad/s . TFR has been proven to be capable of reflecting the locations of scattering centers using Doppler frequency curves [31]. The TFR of the backscattered waves from the target is presented in Fig. 5(a), and that of LGE e_θ is shown in Fig. 6. The backscattered waves used in TFR analysis are under VV polarization and computed by PMLFMA. The TFR method used in this study is a reassigned spectrogram combined with the Wigner-Ville distribution (RSPWVD) [32]. For comparison, the Doppler frequency curves derived by the theoretical locations of the scattering centers are presented in Fig. 5(b).

From Fig. 5 and Fig. 6, the following can be inferred:

- Within $0 < \theta < 20^\circ$, there are two dominant scattering centers: LSC1 and LSC2. They have similar scattering amplitudes and a large separation distance; therefore, large fluctuations are induced in the LGEs.
- Within $20^\circ < \theta < 80^\circ$, the LGEs are induced by SSC and LSC2 because the SSC gradually slides towards LSC2; therefore, the fluctuations in LGEs decrease correspondingly.
- Within $80^\circ < \theta < 100^\circ$, there are four scattering centers. The scattering amplitude of SSC is much larger than that of the other scattering centers; therefore, the LGE is determined mainly by the sliding location of SSC, and consequently, no obvious fluctuation appears.
- Within $100^\circ < \theta < 175^\circ$, relatively large fluctuations are induced in LGEs by LSC2 and LSC3, which have similar scattering amplitudes and a relatively large separation distance. The LGE fluctuations in this region are smaller than those in the $0 < \theta < 20^\circ$ region, where the

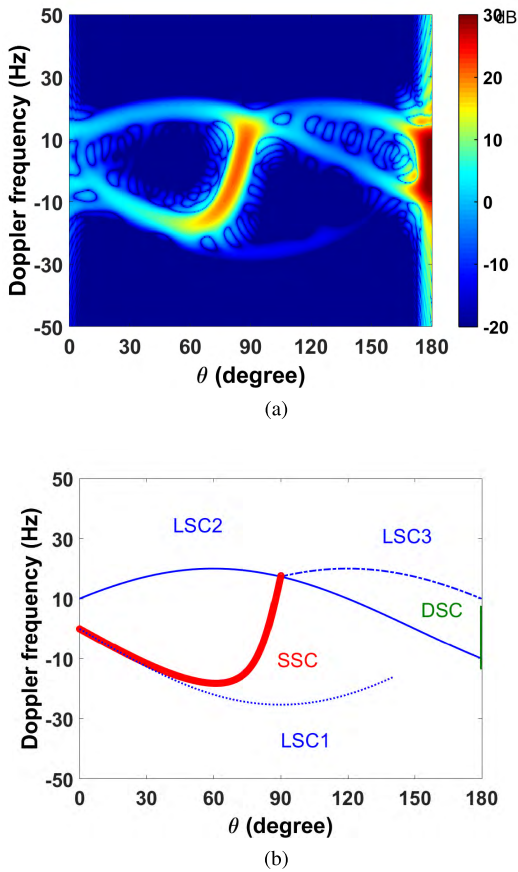


FIGURE 5. The results of the cone with curved generatrix. (a) TFR, (b) Doppler curves derived using theoretical locations.

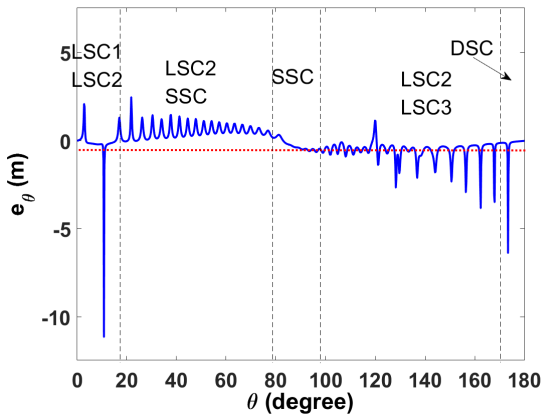


FIGURE 6. LGEs of the cone with curved generatrix.

separation distance of LSC2 and LSC3 is smaller than that of LSC1 and LSC2.

- Within $175^\circ < \theta < 180^\circ$, the LGEs are approximately zero because the DSC is much larger than that of the other scattering centers, LSC2 and LSC3. In addition, it locates at the center of the disk, i.e., the origin of the coordinate systems.

The scattering amplitude of DSC is generally much larger than that of LSCs, either induced by curved edges or apexes.

Therefore, when one DSC and several LSCs appear within a given aspect angle range, the LGEs are determined only by the DSC, and the LSCs cause little interference to the LGEs. When there are one SSC and several LSCs, the LGEs are determined mainly by the SSC, but they might be interfered with, to some extent, by the LSCs, especially when the scattering amplitude of the SSC decreases gradually. When there are only LSCs, highly fluctuating LGEs generally arise because LSCs have similar scattering amplitudes and larger separation distances.

The above cases appropriately explain the negative correlations between LGEs and RCSs of the target; i.e., large LGEs usually appear when the RCS is small. However, there could be exceptions to the common cases, e.g., when multiple DSCs or SSCs exist. Then, highly fluctuating LGEs can arise if they have large separation distances and similar scattering amplitudes.

IV. APPROACH FOR SCATTERING EXTRACTION USING INDUCED CURRENTS

According to scattering theory, scattering centers can be taken as discontinuities in the Stratton-Chu integral equation [33]. These discontinuities are actually the discontinuities of the surface or the curvature of the surface of the illuminated object, such as end points, edges or smooth joints of two surfaces with different curvatures. From the perspective of scattering mechanisms, although the scattering mechanisms at these discontinuities are all diffractions, they are scattering centers of different types because their signatures, as shown in radar images, are quite distinct. Therefore, in scattering center extraction, the currents for different kinds of discontinuities need to be treated differently. In addition, the currents on the continuous surface, such as planar or curved surfaces, have dominant scattering contributions to the total scattered fields of the object and should thus be considered in scattering center extraction.

As shown in Fig. 23 in appendix A, different types of scattering centers can be distributed on different geometric parts of the object. To extract scattering centers from the induced currents on the object, the currents need to first be divided into partitions according to their contributions to the different types of scattering centers.

For LSCs, the contributing currents are those near the end points. The size of the partition (the distance away from the end point) is related to the wavelength (λ) of the incident wave. The typical cases for the partitions of LSCs are shown in Fig. 7, and the size of the partitions for end-points in this work is set to $\frac{\lambda}{10}$.

In this study, DSCs are further classified into three subtypes: DSCP, DSCS and DSCE. DSCP and DSCS are the DSCs induced by the reflection from planar surface and a single-curved surface, respectively, and DSCE is the DSC induced by the diffraction from a straight edge. The contributing currents for DSCP and DSCS are those on the planar surface and the single-curved surface within the light area, respectively. The partitions for DSCP and DSCS are the

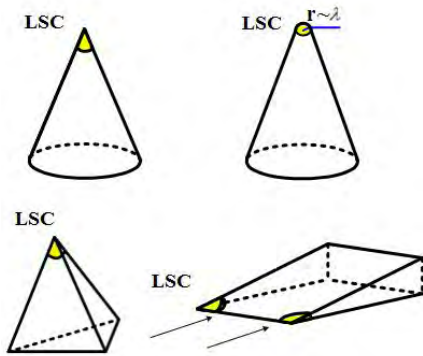


FIGURE 7. Typical cases of partitions for LSCs.

regions on the planar and single-curved surface within the light area after subtracting the partitions for edge and end-point diffractions. The contributing currents for DSCE are the currents along straight edge; therefore, the partition for DSCE is the stripe along the straight edge after subtracting the partitions for LSCs at the end points. The width of the stripe is set as $\frac{\lambda}{10}$. Typical cases for the partitions of DSCs are shown in Fig. 8.

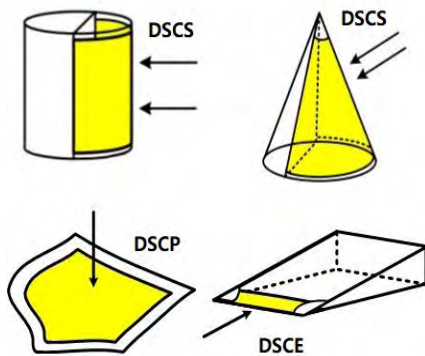


FIGURE 8. Typical cases for the partitions for DSCs.

SSCs are further classified into two subtype:, SSCS and SSCE. An SSCS is the SSC induced by the reflection from a double-curved surface, and an SSCE is the SSC induced by the diffraction from a curved edge. For SSCS and SSCE, their locations slide on the double-curved surface or curved edge with the changes in aspect angle of the LOS. Therefore, the partitions of contributing currents vary with the aspect angle of the LOS. For SSCS, its partition is the stripe along the edge, and the width of the stripe is set as $\frac{\lambda}{10}$. The stripes within light and shadow areas are all considered in this work. The cases for the partitions of SSCs are shown in Fig. 9.

The scattered waves contributed by each partition, i.e., the scattered waves from each scattering center, can be computed by the integral equation for far field conditions shown below:

$$\mathbf{E}_i = DZ\hat{\mathbf{r}}_{los} \times \int_{S'_i} \hat{\mathbf{r}}_{los} \times \mathbf{J}e^{jkr' \cdot \hat{\mathbf{r}}_{los}} ds'_i \quad (15)$$

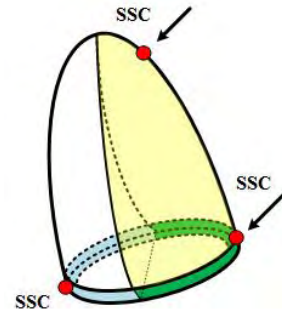


FIGURE 9. The partitions for SSCs.

where $D = jk \frac{e^{-jkr_{los}}}{4\pi r_{los}}$; Z and k are the wave impedance and wave number in free space, respectively; \mathbf{r}' is the location of the current in the local coordinate system; and \mathbf{J} is the current at \mathbf{r}' . S'_i indicates the region of this partition.

The approach for scattering center extraction based on equivalent currents is summarized as follows.

- Step1: Compute the equivalent currents using the full-wave numerical method, and build a data bank of currents under different aspect angles.
- Step2: Divide the geometry of the object into basic geometrical structures, such as planar surfaces, single-curved surfaces, double-curved surfaces, straight edges, curved edges and end points.
- Step3: Select partitions for individual scattering centers according to the geometrical structures, types of scattering centers, and the incident direction of the LOS, as discussed above.
- Step4: Compute the scattering contribution of each partition by using Eq.(15).
- Step5: Check whether the partitions are correct through the Doppler curves shown in the TFRs of the scattered waves. If there are Doppler components of other scattering centers in the TFR, then go to Step3 to modify the corresponding partitions.

The flow chart of the approach is shown in Fig. 10.

To validate this approach, a cone with a curved generatrix and a complex target are investigated here. The complex target is a UAV that is 8.2 m in length and 14.6 m in wingspan (see Fig.11). Taking the UAV as an instance, the process of scattering center extraction is introduced in detail. The parameters used in the computation are as follows: the frequency is 1 GHz; $\theta = \frac{\pi}{2}$; $\phi = 0 \sim \pi$, with a step of 1° ; the total unknowns is 188775; the average length of triangular meshes is 0.1λ; and the polarization is VV. The equivalent currents of the UAV when $\theta = \frac{\pi}{2}$ and $\phi = 0$ are presented in Fig. 12.

The basic structures of the UAV are divided based on the CAD model, as shown in Fig. 13. The structures include the planar surface of the side wings and tail fins, the edges of these wings, the cylindrical surface of the frame, the double-curved surface of the nose, the raised bumps on the frame,

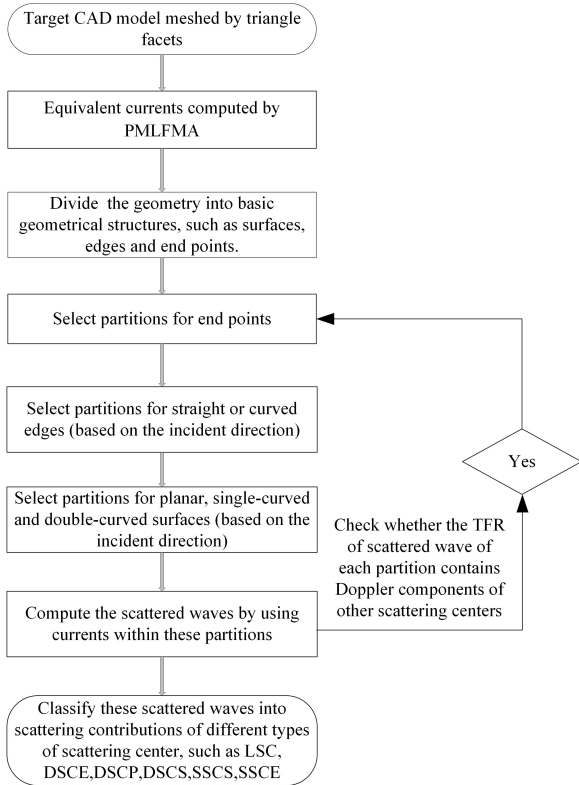


FIGURE 10. The flow chart of this approach.

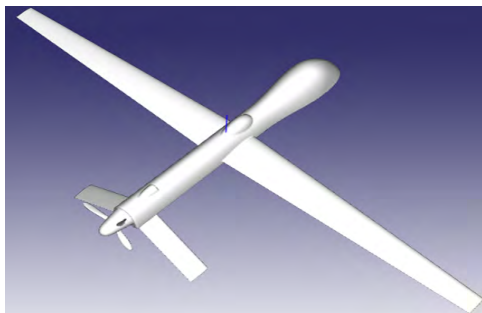


FIGURE 11. The geometry of the UAV.

the planar surfaces of blades and the conical surface of the rotator axis.

The partitions under the aspect angle of the LOS, ($\theta = \frac{\pi}{2}, \phi = \frac{\pi}{6}$), are presented in Fig. 14. Based on the selected partitions, the scattering waves of the corresponding scattering centers can be computed by Eq. (15). Finally, the parametric models of each scattering center are obtained by fitting the numerical results of the scattering contributions to mathematical models. Under the given observation range, 23 scattering centers are considered and extracted by this approach, including 6 DSCs, 3 SSCs and 14 LSCs. Compared with the commonly used inverse method, in which the parameters are estimated from the total fields, it is easier to estimate the parameters of the scattering centers from their individual scattering contributions because the interference from other scattering centers is effectively avoided. That is,

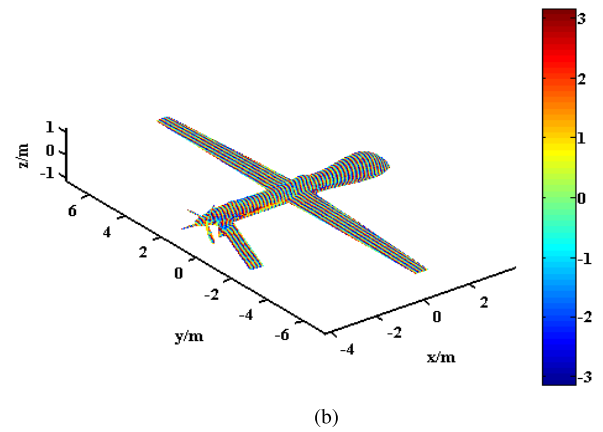
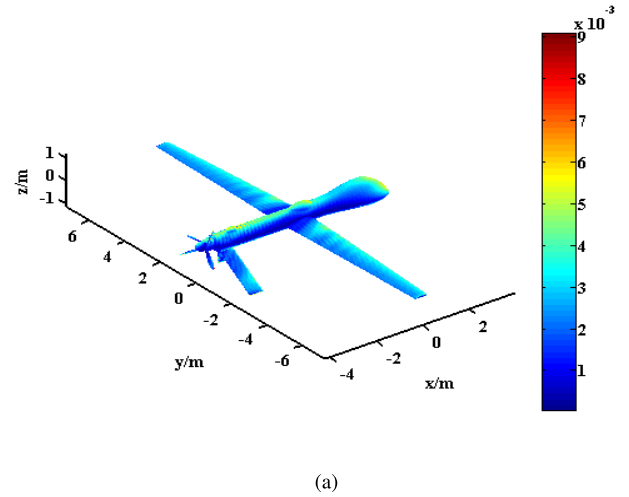


FIGURE 12. The equivalent currents (a) in amplitudes, (b) in phases.

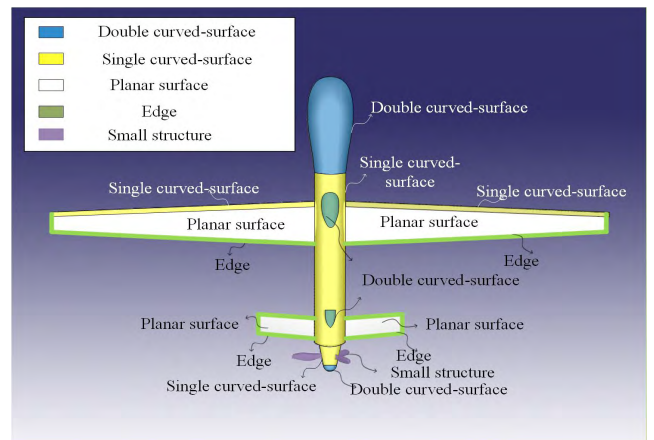


FIGURE 13. The basic geometrical structures of the UAV.

when estimating parameters from the TFR of the total fields, the estimation errors induced by serious cross-terms can be avoided.

A. THE SCATTERING CENTER MODELING OF DSCs

The DSC on the front edge of the side wing is investigated here to illustrate the process of function fitting. The

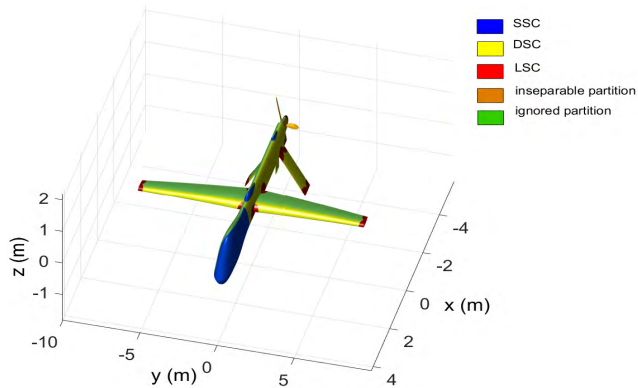


FIGURE 14. The partitions for the scattering centers.

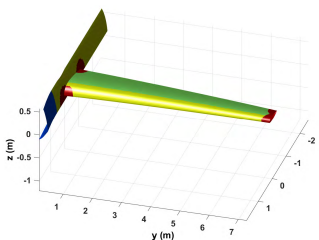


FIGURE 15. The partition for the DSC on the front-edge of the side wing.

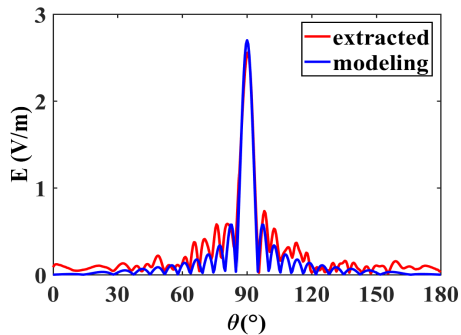


FIGURE 16. The aspect dependence of the DSC and the fitted model using the sinc function.

variation of the scattering amplitude of the DSC with the change in aspect angle is shown in Fig. 16. In the existing scattering center models, the scattering fields by DSCs can be expressed by Eq. (16). The fitted result is also presented in Fig. 16.

$$E_{DSC} = j^\alpha e^{j\varphi} e^{jk\mathbf{r}' \cdot \hat{\mathbf{r}}_{los}} A(\Psi) \quad (16)$$

where

$$A(\Psi) = C_1 |\cos(\Psi - \Psi_1)| \text{sinc}[kC_2 \sin(\Psi - \Psi_1)] \quad (17)$$

where $C_1, C_2, \Psi_1, \varphi, \alpha$ are real values to be estimated. \mathbf{r}' is the position vector of the center of the partition.

Similarly, the other DSCs are modeled by using the sinc function in the following analysis.

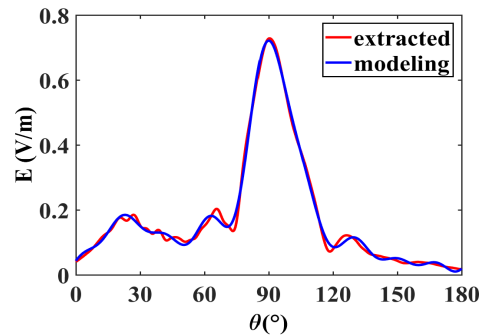


FIGURE 17. The scattering amplitude of the LSC and the fitted result.

B. THE SCATTERING CENTER MODELING OF LSCs

The LSC on the end-point of the side wing is investigated here as an example. The scattering amplitude of the LSC with the change in aspect angle is shown in Fig. 17. Considering the aspect dependency of LSC is far more complex than the commonly used damped exponential function; thus, the parametric models of LSCs are expressed by rational polynomial functions in this work, as expressed by Eq. (19). The fitted result is presented in Fig. 17 for comparison. The other LSCs are modeled similarly.

$$E_{LSC} = j^\alpha e^{j\varphi} e^{jk\mathbf{r}' \cdot \hat{\mathbf{r}}_{los}} A(\Psi) \quad (18)$$

where

$$A(\xi) = \frac{\sum_{p=0}^m P_p^i \xi^p}{\sum_{q=0}^{n-1} Q_q^i \xi^q + \xi^n}, \quad (19)$$

where P_p^i, Q_q^i are the coefficients of the function and m, n are the orders. \mathbf{r}' is the position vector of the end point of the edge.

The higher the order is, the more complex function can be described. However, higher orders result in more complex parametric models, longer fitting times and a higher risk of local minima. According to the change of scattering amplitude of the LSC, the optimal polynomial orders are determined to be $n = 9$ and $m = 8$, through a process of trial and error.

C. THE SCATTERING CENTER MODELING OF SSCs

The SSC on the nose is investigated as an example. The scattering amplitude of the SSC with the change in aspect angle is shown in Fig. 18. The curvature of the double-curved surface is unknown, so the aspect dependent function of SSC ($A(\Psi)$) is expressed in Eq. (19). Then, the parametric model of SSC can be expressed by Eq. (20).

$$E_{SSC1} = A(\Psi) \exp(jk\mathbf{r}'(\Psi) \cdot \hat{\mathbf{r}}_{los}) \quad (20)$$

where \mathbf{r}' is the position vector of the point of specular reflection and can be calculated according to the relation between the normal direction and the incident direction [10].

The fitted result is presented in Fig. 18 for comparison. The other SSCs are also modeled similarly.

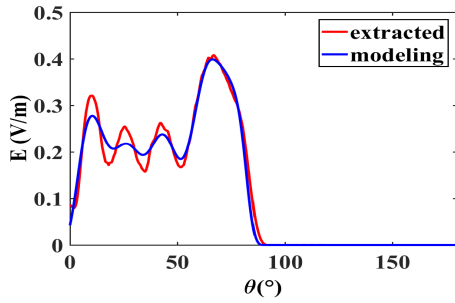


FIGURE 18. The scattering amplitude of the SSC and the fitted result.

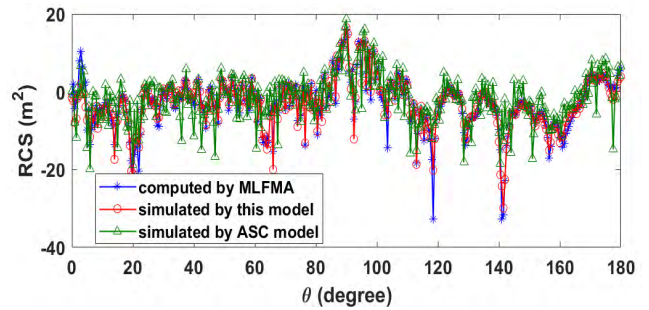


FIGURE 20. The comparison between the RCSs computed by the models and those computed by PMLFMA and the ASC model.

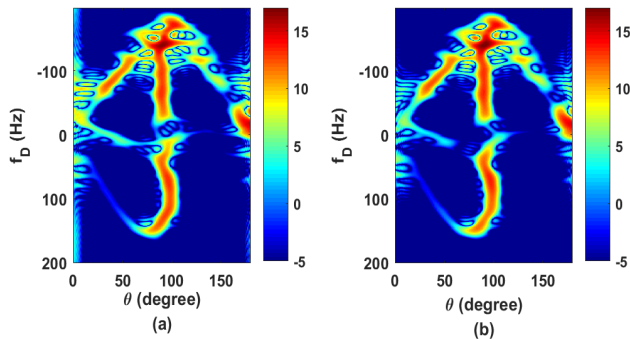


FIGURE 19. The comparison between the TFRs computed by these models and those computed by PMLFMA.

Finally, the total fields are computed by adding up the contributions of all the scattering centers. For the UAV, the cross-correlation coefficient between the TFR simulated by these models, and that computed by PMLFMA is 95%. The two TFRs are shown in Fig. 19. The RMSE between the RCSs simulated by the models and those of PMLFMA is 2.14 dB. For comparison, the attributed scattering center (ASC) model is obtained through the inverse approach, which involves directly estimating the parameters of the models from the TFR of the total fields by using GA [19], [34]. The RMSE between the RCSs of the ASC model and those computed by PMLFMA is 4.25 dB, and the cross-correlation coefficient of the two TFRs is 81%. The RCSs simulated by the models, the ASC model, those computed by PMLFMA and those obtained by inverse estimation are presented in Fig. 20 for comparison. The results for the cone with curved generatrix are presented in appendix C.

V. VALIDATION OF THE SIMULATION OF LGEs

Based on the models of scattering centers and the derived LGE formulae, the LGEs of the UAV are computed and compared with the results obtained using brute-force computation, as shown in Fig. 21. From this figure, it can be seen that the results simulated by the formulae agree with those computed by PMLFMA. The RMSE of e_θ of the two methods is 1.27 m, and the cross-coefficient of the two results is 86.3%. The statistical distributions of LGEs of these models and those of PMLFAM are presented in Fig. 22,

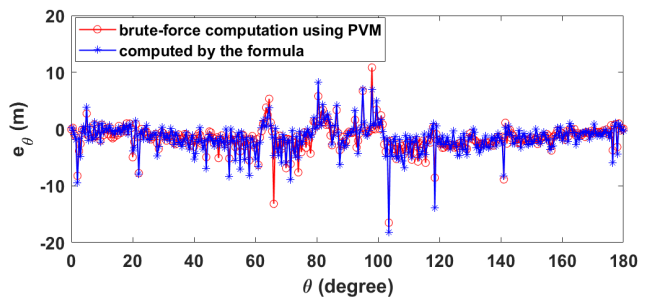


FIGURE 21. LGEs of the UAV.

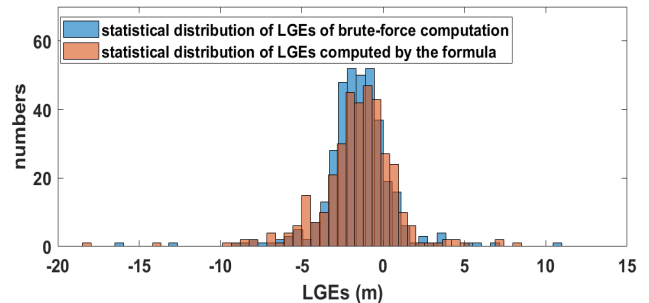


FIGURE 22. Statistical distribution of the LGEs.

TABLE 1. Time-consumption comparison.

computing scattered fields on parallel servers ($\theta = 0 : 1^\circ : 180^\circ$)	13.72 h
brute-force LGEs on parallel servers ($\theta = 0 : 1^\circ : 180^\circ$)	13.72 h
computing LGEs using this model on a PC ($\theta = 0 : 0.2^\circ : 180^\circ$)	3 s
brute-force LGEs on parallel servers ($\theta = 0 : 0.2^\circ : 180^\circ$)	54.9 h

which shows good agreement between our models with those of PMLFMA.

It is well known that using scattering center models, if they are readily available, is more efficient than using a brute-force computation of the scattered fields in a simulation. The scattering center model used for LGE simulation is not as readily available as those used for radar imaging simulation because of the higher precision required for

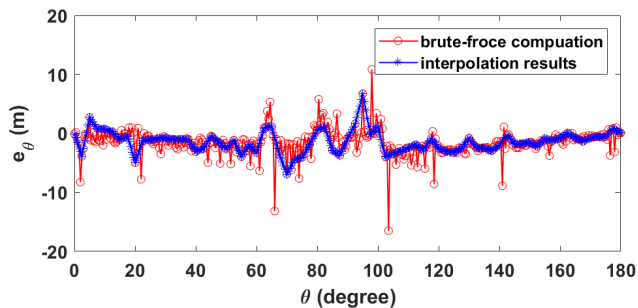


FIGURE 23. LGEs of the UAV obtained by interpolation.

Type	Locations of scattering centers
LSC	
DSC	
SSC	

FIGURE 24. Locations of scattering centers on geometric structures.

LGE simulation. Therefore, to ensure that the precision of scattering centers is sufficiently high for LGE simulation, full-wave numerical results are used here during the process of scattering center modeling. Although full-wave numerical computation is also used in scattering modeling, the scattering center model developed in sparse aspect angles can be used to simulate LGEs in the dense aspect angles required for complex targets, which still gives a high efficiency for simulating LGEs.

Using these models, LGEs at dense aspect angles can be computed in real time by a PC. However, they can hardly be obtained by interpolation based on the known LGEs since the LGEs fluctuate drastically with changes in the aspect angle. Therefore, using brute-force computation, the cumbersome scattering field solution must be repeated on parallel servers. The time cost of the two procedures, e.g., for the UAV, are listed in Table 1. The configurations of the PC and sever are DELL 3668-R2938, CPU, i7-7700, IBM System x3650M5, and CPU 2.2 GHz. The computation time for one aspect angle using 24 parallel threads is 262 s. The errors induced by interpolation are shown in Fig. 23, where the original LGEs are at 0 ~ 180° with a step of 1°, and the step angle of simulated LGEs is 0.2°. Fig. 23 shows large errors between the statistical distribution of LGEs computed by interpolation and those that are directly computed. The RMSE of e_θ of the two methods is 2.11 m, and the cross-coefficient of the two results is 49.8%.

VI. CONCLUSIONS

LGE formulae are derived for complex targets with attributed scattering center in this work. The LGE simulation based on the derived formulae requires a higher precision scattering center model than radar imaging simulation does because the fluctuations of the LGEs are more sensitive to the locations and amplitudes of the attributed scattering centers. An approach using induced currents on targets is presented to acquire highly precise scattering center parameters. The scattering center model using full wave numerical results in sparse aspect angles can be used to accurately simulate LGE in dense aspect angles, which gives a high efficiency for simulating LGE for complex targets. LGEs of a UVA with 23 scattering centers are investigated for validation. Comparisons of the LEG simulation using this model with numerical results obtained by brute-force computation establish the feasibility and precision of the proposed approach.

APPENDIX A

LSCs are induced by waves diffracted from geometric discontinuities, such as corners and the apexes of edges. They can be observed in a wide range of aspect angles and are located at the position of discontinuity. DSCs are induced by waves reflected from a planar or single-curved surface, or by waves diffracted from a straight edge. They can be observed only when the LOS of radar is vertical to the surface or edge and is distributed throughout the reflecting surface or edge. SSCs are induced by waves reflected from a curved surface or by waves diffracted from a curved edge. They can be observed in a wider range of aspect angles than that of DSCs, and their locations slide continuously along the curved surface or edge with changes in the aspect angle. Based on the formation mechanisms, the locations of LSC, DSC and SSC can be derived according to the geometry of the object, as illustrated in Fig. 23.

APPENDIX B

The average Poynting vector can be expressed as

$$\begin{aligned} \mathbf{P} &= \frac{1}{2} Re[\mathbf{E} \times \mathbf{H}^*] \\ &= \frac{1}{2\eta_0} \sum_i^n \sum_j^n \frac{A_i A_j}{R_i R_j} \left(\frac{f}{f_c}\right)^{\alpha_i + \alpha_j} \cos \Omega(\cdot) \hat{\mathbf{k}}_{ij} \end{aligned} \quad (21)$$

where

$$\Omega(\cdot) = \cos[2k(R_j - R_i) + \frac{\pi}{2}(\alpha_i - \alpha_j) + \varphi_i - \varphi_j] \quad (22)$$

$$\hat{\mathbf{k}}_{ij} = \cos \theta_j \cos(\phi_i - \phi_j) \hat{\mathbf{z}} + \sin \theta_i \sin \phi_j \hat{\mathbf{y}} + \sin \theta_i \cos \phi_j \hat{\mathbf{x}} \quad (23)$$

Due to the superposition of electric and magnetic fields in the scattered waves from multiple scattering centers, the direction of the average Poynting vector deviates from the direction of the wave propagation from target to radar, i.e., $\hat{\mathbf{r}}_{los}$, as illustrated in Fig.1.

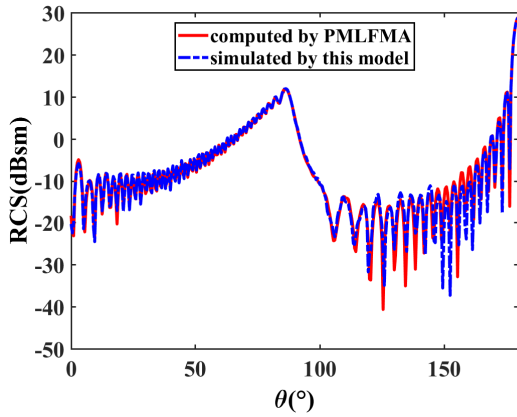


FIGURE 25. The RCSs of the cone with curved generatrix.

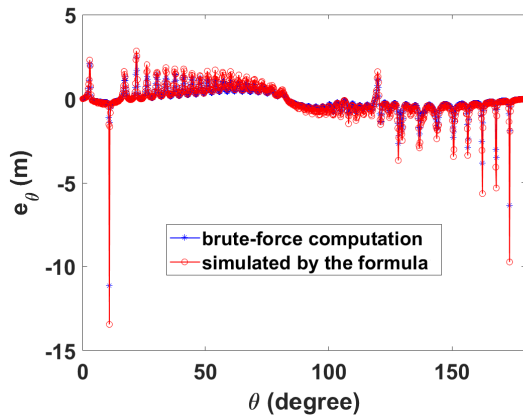


FIGURE 26. The LGEs of the cone with curved generatrix.

The angle between $\hat{\mathbf{r}}_{los}$ and \mathbf{P} is the glint angle, and the distance error induced by the glint angle is the distance between o and o' . Generally, the projection distances of oo' along the $\hat{\theta}_{los}$ and $\hat{\phi}_{los}$ directions are the LGEs, denoted by e_θ and e_ϕ , respectively.

The components of \mathbf{P} along $\hat{\mathbf{r}}_{los}$, $\hat{\theta}_{los}$ and $\hat{\phi}_{los}$ can then be derived as

$$P_r = \mathbf{P} \cdot \hat{\mathbf{r}}_{los} = \sin \theta_{los} P_1 + \cos \theta_{los} P_2 \quad (24)$$

$$P_\theta = \mathbf{P} \cdot \hat{\theta}_{los} = \cos \theta_{los} P_1 - \sin \theta_{los} P_2 \quad (25)$$

$$P_\phi = \mathbf{P} \cdot \hat{\phi}_{los} = \cos \phi_{los} P_{11} - \sin \phi_{los} P_{12} \quad (26)$$

where

$$P_1 = \frac{1}{2\eta_0} \sum_i^n \sum_j^n g_{ij} \sin \theta_i \cos(\phi_j - \phi_{los}) \quad (27)$$

$$P_2 = \frac{1}{2\eta_0} \sum_i^n \sum_j^n g_{ij} \cos \theta_i \cos(\phi_i - \phi_j) \quad (28)$$

$$P_{11} = \frac{1}{2\eta_0} \sum_i^n \sum_j^n g_{ij} \sin \theta_i \sin \phi_j \quad (29)$$

$$P_{12} = \frac{1}{2\eta_0} \sum_i^n \sum_j^n g_{ij} \sin \theta_i \cos \phi_j, \quad (30)$$

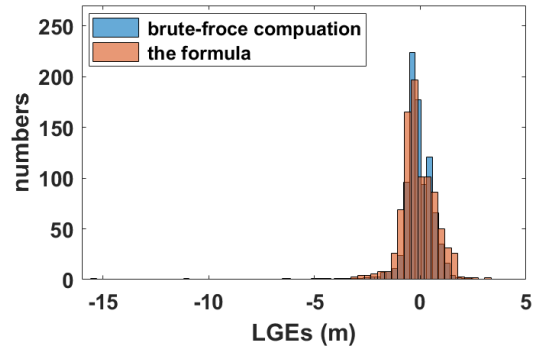


FIGURE 27. The statistical distribution of the LGEs.

where

$$g_{ij} = \frac{A_i A_j}{R_i R_j} \left(\frac{f}{f_c}\right)^{(\alpha_i + \alpha_j)} \cos \Omega(\cdot). \quad (31)$$

Let

$$\tan \Theta = \frac{P_1}{P_2}; \tan \Phi = \frac{P_{11}}{P_{12}}, \quad (32)$$

Then, the LGEs can be derived as

$$e_\theta = r_{los} \frac{P_\theta}{P_r} = r_{los} \tan(\Theta - \theta_{los}) \quad (33)$$

$$e_\phi = r_{los} \frac{P_\phi}{P_r} = r_{los} \frac{\sin \Theta \tan(\Phi - \phi_{los})}{\cos(\Theta - \theta_{los})} \quad (34)$$

APPENDIX C

The RCSs of the cone with curved generatrix simulated by the developed models are compared with those computed by PMLFMA, as shown in Fig. 25. The RMSE of RCSs is 1.23 dB. The LGEs simulated by the formula are compared with those computed by brute-force computation, as shown in Fig. 26. The RMSE of LEGs is 0.29 m, and their cross-coefficient is 94%. The statistical distribution of the two results of LGEs agree well with each other, as shown in Fig. 27.

REFERENCES

- [1] Z. Jianxiang, S. Zhiguang, C. Xiao, and F. Qiang, "Automatic target recognition of SAR images based on global scattering center model," *IEEE Trans. Geosci. Remote Sens.*, vol. 49, no. 10, pp. 3713–3729, Oct. 2011.
- [2] M. C. Hui, W. G. Jian, H. X. Hong, Y. X. Liang, and D. BaiYuan, "Scatterer-based approach to evaluate similarity between 3D EM-model and 2D SAR data for ATR," *IET Radar Sonar Navigat.*, vol. 11, no. 2, pp. 254–259, Feb. 2017.
- [3] B. Ding, G. Wen, X. Huang, C. Ma, and X. Yang, "Data augmentation by multilevel reconstruction using attributed scattering center for SAR target recognition," *IEEE Geosci. Remote Sens. Lett.*, vol. 14, no. 6, pp. 979–983, Jun. 2017.
- [4] M. Hurst and R. Mittra, "Scattering center analysis via Prony's method," *IEEE Trans. Antennas Propag.*, vol. AP-35, no. 8, pp. 986–988, Aug. 1987.
- [5] R. Carriere and R. L. Moses, "High resolution radar target modeling using a modified Prony estimator," *IEEE Trans. Antennas Propag.*, vol. 40, no. 1, pp. 13–18, Jan. 1992.
- [6] L. C. Potter, D.-M. Chiang, R. Carriere, and M. J. Gerry, "A GTD-based parametric model for radar scattering," *IEEE Trans. Antennas Propag.*, vol. 43, no. 10, pp. 1058–1067, Oct. 1995.
- [7] L. C. Potter and R. L. Moses, "Attributed scattering centers for SAR ATR," *IEEE Trans. Image Process.*, vol. 6, no. 1, pp. 79–91, Jan. 1997.

- [8] M. J. Gerry, L. C. Potter, I. J. Gupta, and A. Van Der Merwe, "A parametric model for synthetic aperture radar measurements," *IEEE Trans. Antennas Propag.*, vol. 47, no. 7, pp. 1179–1188, Jul. 1999.
- [9] J. A. Jackson, B. D. Rigling, and R. L. Moses, "Canonical scattering feature models for 3D and bistatic SAR," *IEEE Trans. Aerosp. Electron. Syst.*, vol. 46, no. 2, pp. 525–541, Apr. 2010.
- [10] K.-Y. Guo, Q.-F. Li, X.-Q. Sheng, and M. Gashinova, "Sliding scattering center model for extended streamlined targets," *Prog. Electromagn. Res.*, vol. 139, pp. 499–516, 2013.
- [11] L. Ma, J. Liu, T. Wang, Y. Li, and X. Wang, "Micro-Doppler characteristics of sliding-type scattering center on rotationally symmetric target," *Sci. China Inf. Sci.*, vol. 54, no. 9, pp. 1957–1967, 2011.
- [12] Q.-Y. Qu, K.-Y. Guo, and X.-Q. Sheng, "An accurate bistatic scattering center model for extended cone-shaped targets," *IEEE Trans. Antennas Propag.*, vol. 62, no. 10, pp. 5209–5218, Oct. 2014.
- [13] R. Bhalla and H. Ling, "Three-dimensional scattering center extraction using the shooting and bouncing ray technique," *IEEE Trans. Antennas Propag.*, vol. 44, no. 11, pp. 1445–1453, Nov. 1996.
- [14] R. Bhalla, J. Moore, and H. Ling, "A global scattering center representation of complex targets using the shooting and bouncing ray technique," *IEEE Trans. Antennas Propag.*, vol. 45, no. 12, pp. 1850–1856, Dec. 1997.
- [15] J. Zhou, Z. Shi, and Q. Fu, "Three-dimensional scattering center extraction based on wide aperture data at a single elevation," *IEEE Trans. Geosci. Remote Sens.*, vol. 53, no. 3, pp. 1638–1655, Mar. 2015.
- [16] Y. Cong, B. Chen, H. Liu, and B. Jiu, "Nonparametric Bayesian attributed scattering center extraction for synthetic aperture radar targets," *IEEE Trans. Signal Process.*, vol. 64, no. 18, pp. 4723–4736, Sep. 2016.
- [17] X. Wang, M. Zhang, and J. Zhao, "Efficient cross-range scaling method via two-dimensional unitary ESPRIT scattering center extraction algorithm," *IEEE Geosci. Remote Sens. Lett.*, vol. 12, no. 5, pp. 928–932, May 2015.
- [18] J. Hu, W. Wang, Q. Zhai, J. Ou, R. Zhan, and J. Zhang, "Global scattering center extraction for radar targets using a modified RANSAC method," *IEEE Trans. Antennas Propag.*, vol. 64, no. 8, pp. 3573–3586, Aug. 2016.
- [19] Q. Li, E. J. Rothwell, K.-M. Chen, and D. P. Nyquist, "Scattering center analysis of radar targets using fitting scheme and genetic algorithm," *IEEE Trans. Antennas Propag.*, vol. 44, no. 2, pp. 198–207, Feb. 1996.
- [20] Y. He, S.-Y. He, Y.-H. Zhang, G.-J. Wen, D.-F. Yu, and G.-Q. Zhu, "A forward approach to establish parametric scattering center models for known complex radar targets applied to SAR ATR," *IEEE Trans. Antennas Propag.*, vol. 62, no. 12, pp. 6192–6205, Dec. 2014.
- [21] S.-Y. Wang and S.-K. Jeng, "A deterministic method for generating a scattering-center model to reconstruct the RCS pattern of complex radar targets," *IEEE Trans. Electromagn. Compat.*, vol. 39, no. 4, pp. 315–323, Nov. 1997.
- [22] D. D. Howard, "Radar target glint in tracking and guidance system based on echo signal phase distortion," in *Proc. NEC*, vol. 15, 1959, pp. 840–849.
- [23] P. J. Kajenski, "Comparison of two theories of angle glint: Polarization considerations," *IEEE Trans. Aerosp. Electron. Syst.*, vol. 42, no. 1, pp. 206–210, Jan. 2006.
- [24] H. C. Yin and P. K. Huang, "Further comparison between two concepts of radar target angular glint," *IEEE Trans. Aerosp. Electron. Syst.*, vol. 44, no. 1, pp. 372–380, Jan. 2008.
- [25] R. A. Ross and M. E. Bechtel, "Scattering-center theory and radar glint analysis," *IEEE Trans. Aerosp. Electron. Syst.*, vol. AES-4, no. 5, pp. 756–762, Sep. 1968.
- [26] M. B. Schober, "Angular mean and variance for selected two-source radar-target combinations," *IEEE Trans. Aerosp. Electron. Syst.*, vol. 38, no. 3, pp. 1038–1046, Jul. 2002.
- [27] Y. Hong-Cheng, W. Chao, and H. Pei-Kang, "Inherent relations among the three representations of radar target angular glint," (in English), *J. Radars*, vol. 3, no. 2, pp. 119–128, 2014.
- [28] M. Sui and X. Xu, "Angular glint calculation and analysis of radar targets via adaptive cross approximation algorithm," *J. Syst. Eng. Electron.*, vol. 25, no. 3, pp. 411–421, Jun. 2014.
- [29] X. M. Pan and X. Q. Sh, "A sophisticated parallel MLFMA for scattering by extremely large targets [EM programmer's notebook]," *IEEE Antennas Propag. Mag.*, vol. 50, no. 3, pp. 129–138, Jun. 2008.
- [30] K.-Y. Guo, Q.-Y. Qu, and X.-Q. Sheng, "Geometry reconstruction based on attributes of scattering centers by using time-frequency representations," *IEEE Trans. Antennas Propag.*, vol. 64, no. 2, pp. 708–720, Feb. 2016.
- [31] V. C. Chen and H. Ling, *Time-Frequency Transforms for Radar Imaging and Signal Analysis*. Norwood, MA, USA: Artech House, 2002.
- [32] F. Auger and P. Flandrin, "Improving the readability of time-frequency and time-scale representations by the reassignment method," *IEEE Trans. Signal Process.*, vol. 43, no. 5, pp. 1068–1089, May 1995.
- [33] H. E. G. Jeske, *Atmospheric Effects on Radar Target Identification and Imaging*. Amsterdam, The Netherlands: Reidel, 1976.
- [34] E. J. Hughes and M. Leyland, "Using multiple genetic algorithms to generate radar point-scatterer models," *IEEE Trans. Evol. Comput.*, vol. 4, no. 2, pp. 147–163, Jul. 2000.

KUN-YI GUO (M'14) received the Ph.D. degree from the Institute of electronics, Chinese Academy of Sciences. In 2005, she joined the Center for Electromagnetic Simulation, Beijing Institute of Technology (BIT), where she is currently an Associate Professor with the School of Information And Electronics. Her current research interests include electromagnetic scattering, antenna propagation, and radar signal processing. She was a fourth recipient of the First Prize of the Beijing Science and Technology Awards in 2009. She received the Excellent Young Teacher Project of BIT from 2010 to 2013.

GUANG-LIANG XIAO was born in Loudi, Hunan, China, in 1992. He received the B.S. degree in electrical engineering from the Beijing Institute of Technology, Beijing, China, in 2015, where he is currently pursuing the Ph.D. degree in the electromagnetics and microwave technology. His current research interests include electromagnetic scattering and computational electromagnetics.

YUN ZHAI was born in Beijing, China, in 1992. She received the B.S. degree in information engineering from the Nanjing University of Aeronautics and Astronautics, Jiangsu, China, in 2014, and the M.S. degree in electrical engineering from the Beijing Institute of Technology, Beijing, China, in 2017. Her current research interests include electromagnetic scattering and radar signal processing.

XIN-QING SHENG (SM'10) received the B.S., M.S., and Ph.D. degrees from the University of Science and Technology of China, Hefei, China, in 1991, 1994, and 1996, respectively. He has authored or co-authored over 120 papers in refereed journals and three books *Essentials of Computational Electromagnetics* (Singapore: IEEE Press-Wiley, 2012), *A Brief Treatise on Computational Electromagnetics* (Beijing: Science Press, 2004), and *A Treatise on Electromagnetic Wave* (Beijing: Science Press, 2007). He has authored SINOCOM, simulation software for scattering by complex targets. He is currently a Chang-Jiang Professor with the School of Information and Electronic, Beijing Institute of Technology. His research interests include computational electromagnetics, scattering and antenna analysis, electromagnetic compatibility, and microwave imaging. He was a recipient of the 2001 One Hundred Talents Program from the Chinese Academy of Sciences, the 2004 Cheung Kong Scholar Program from the Ministry of Education of China, and the first recipient of the First Prize of the Beijing Science and Technology Awards in 2009.

• • •